Nanolaminate Nano-Optoelectrodes Enable Dual-Channel Plasmon-Enhanced Raman Spectroscopy for Electrochemistry

*Yuming Zhao, Elieser Mejia, Chuan Xiao, Junyeob Song, Wenqi Zhu, Henri Lezec, Amit Agrawal, and Wei Zhou**

In situ monitoring of short-lived transition states (TSs) is crucial for understanding electrochemical reaction mechanisms but remains challenging. Conventional electrochemical surface-enhanced Raman spectroscopy (EC-SERS) primarily provides vibrational information, with limitations in hotspot reproducibility and often overlooking electronic information associated with TSs. This study introduces a dual-channel EC-SERS strategy using nanolaminate nano-optoelectrode (NLNOE) devices, integrating plasmon-enhanced vibrational Raman scattering (PE-VRS) and plasmon-enhanced electronic Raman scattering (PE-ERS) to concurrently probe TS dynamics within electrically connected plasmonic nanocavities. Using the $AgCl(s) + e^- \rightleftharpoons Ag(s) + Cl^-(aq)$ redox system, this approach distinct PE-VRS and PE-ERS signatures of the $(AgCl)^*$ TS. Notably, a significant increase in PE-ERS signals concurrent with $(AgCl)^*$ TS emergence, characterized by filled bonding and unoccupied antibonding orbitals with negligible energy gaps. This enhanced PE-ERS signal correlates with increased $(AgCl)^*$ TS polarizability, leading to amplified PE-VRS signals due to enhanced electron cloud distortion. By modulating Cl^- ion concentrations via electrolyte composition (1× PBS and 1× PBS-equivalent KH_2PO_4) while maintaining constant total ion concentration, the competition between Ag/AgCl and Ag/AgH_2PO_4 redox reactions within Ag nanolayers is influenced. These results demonstrate the capability of dual-channel EC-SERS to distinguish interfacial redox reactions based on distinct electronic and vibrational signatures associated with covalent and ionic bond characteristics.

1. Introduction

Understanding the mechanisms that drive electrochemical reactions hinges on the ability to study transition states (TSs)—the short-lived, high-energy molecular configurations in the reaction pathway.[1–4] While recent advances in spectroscopy[5,6] and computational modeling[3,7] have provided valuable insights into TSs, directly observing these transient species in real time remains a significant challenge. This challenge is particularly severe for interfacial electrochemical reactions, which occur within nanometer-thin layers at the electrode-electrolyte interface[3,8] and are crucial for applications ranging from catalysis[9] and biosensing[10] to energy conversion.[11] The confined spatial extent and fleeting nature of TSs demand highly sensitive detection techniques capable of discerning weak signals amidst background noise from the bulk electrolyte and electrode.[12,13]

Surface plasmon-enhanced spectroelectrochemistry has emerged as a promising approach to amplify the sensitivity of optical probes for interfacial studies.[14–16] Through nanolocalized enhancement of optical fields at metal-dielectric interfaces,[17] surface plasmons amplify the local density of optical states, thereby enhancing various nonlinear luminescence processes, including fluorescence, Raman scattering, and harmonic generation.[18–26] The integration of plasmonics with spectroelectrochemistry

---

Y. Zhao, E. Mejia, C. Xiao, W. Zhou
Department of Electrical and Computer Engineering
Virginia Tech
Blacksburg, VA 24061, USA
E-mail: wzh@vt.edu

The ORCID identification number(s) for the author(s) of this article can be found under https://doi.org/10.1002/smtd.202402107

DOI: 10.1002/smtd.202402107

E. Mejia, J. Song, W. Zhu, H. Lezec
Physical Measurement Laboratory
National Institute of Standards and Technology (NIST)
Gaithersburg, MD 20899, USA

A. Agrawal
Department of Engineering
University of Cambridge
Cambridge CB3 0FA, UK

A. Agrawal
Kyung Hee University
26 Kyungheedae-ro, Dongdaemun-gu, Seoul 02447, South Korea

offers the potential to monitor interfacial electrochemical activities with unprecedented sensitivity. While time-resolved studies using plasmonic nanostructures coupled with ultrafast spectroscopy have been pivotal in advancing our understanding of chemical dynamics,[27–30] existing pump-probe methods often rely on pulsed optical excitation,[31,32] This reliance poses a limitation for directly tracking short-lived TSs in electrochemical reactions, which require precisely timed electrical modulation to initiate and control the reaction kinetics.[33]

Electrochemical surface-enhanced Raman spectroscopy (EC-SERS) has become a widely used spectroelectrochemistry technique for investigating interfacial electrochemical processes,[34–43] even enabling the detection of semi-stable intermediate states.[44,45] Nevertheless, the application of EC-SERS for probing highly transient TSs remains unexplored. Moreover, conventional EC-SERS predominantly provide vibrational information,[37–42,44,45] limiting their ability to probe interfacial electronic state changes accompanying interfacial reactions. Past EC-SERS studies often overlook the voltage-modulated metal luminescence signals with plasmon enhancement[46] and suffer from inconsistent and unstable plasmonic hotspots,[37–42] hindering the reliability and reproducibility of measurements.

This study presents an in situ dual-channel EC-SERS methodology that synergizes plasmon-enhanced vibrational Raman scattering (PE-VRS) with plasmon-enhanced electronic Raman scattering (PE-ERS). This approach uniquely enables the simultaneous monitoring of both vibrational and electronic transitions associated with TSs within electrochemically active plasmonic nanocavities. By employing nanolaminate nano-optoelectrode (NLNOE) devices, which feature electrically connected, spatially uniform, and mechanically robust plasmonic hotspots, we achieve highly sensitive and reproducible detection of TS dynamics. Utilizing the $AgCl(s) + e^- \rightleftharpoons Ag(s) + Cl^-(aq)$ redox system on Au/Ag NLNOEs, we demonstrated the efficacy of this dual-channel EC-SERS approach in capturing correlated vibrational and electronic Raman signatures of the $(AgCl)^*$ TSs. Our findings reveal a significant increase in PE-ERS signals during interfacial redox reactions concurrent with the emergence of $(AgCl)^*$ TSs, characterized by filled bonding and unoccupied antibonding orbitals with negligible energy gaps. Additionally, the observation of increased PE-VRS signals during the redox reaction reveals that the $(AgCl)^*$ TS with partial bonding can increase electron cloud distortion under laser excitation to elevate Raman cross-section and PE-VRS signals. Furthermore, we observe a temporal discrepancy between the electrochemical current and the PE-ERS/PE-VRS emission patterns, which we ascribe to spatial variations in plasmonic field enhancement factors within the Au-Ag-Au nanogap's porous Ag/AgCl networks formed during the redox reaction. To further explore the versatility and universality of our dual-channel EC-SERS methodology, we conducted in situ EC-SERS measurements with Au-sidewall-coated Au-Ag-Au NLNOE devices under different chemical environments. By varying the electrolyte composition (1× PBS and 1× PBS-equivalent KH_2PO_4) while maintaining a constant total ion concentration, we modulated the relative concentrations of Cl^- ions, thereby influencing the competition between Ag/AgCl and Ag/AgH_2PO_4 redox reactions within the Ag nanolayers. Our results demonstrate the capability of the dual-channel EC-SERS approach to distinguish different interfacial redox reactions based on the distinct electronic and vibrational signatures associated with covalent and ionic bond characteristics. This expanded capability highlights the broad applicability of our methodology for investigating interfacial redox reactions in diverse electrochemical systems.

2. Results and Discussion

Recent studies[47–49] have revealed that PE-ERS primarily accounts for the low-wavenumber background in SERS measurements from noble metal nanocavity hotspots under continuous wave (CW) laser excitation at near-infrared (NIR) wavelengths, as the interband transitions[50,51] do not occur by low photon energy and intraband transitions[52,53] are unlikely due to momentum mismatch from sp-band dispersion. PE-ERS signals in metal originate from the electron-hole pair transitions near the Fermi energy E_F (**Figure 1A**), with intensity proportional to $n_{e-h}(\Delta\omega) \propto n(E_F)|\exp(-\frac{\hbar\Delta\omega}{k_BT}) - 1|^{-1}$, where $n(E_F)$ denotes the free electron density and $|\exp(-\frac{\hbar\Delta\omega}{k_BT}) - 1|^{-1}$ is the Bose-Einstein distribution of the electron-hole pairs at Raman-shift frequency $\Delta\omega$. Utilizing a long-pass filter to eliminate elastic laser scattering, we obtain a PE-ERS pseudo peak in the spectra (Figure 1A, bottom).[48] In contrast to the continuous nature of PE-ERS signals, PE-VRS signals exhibit discrete peaks due to inelastic scattering involving distinct molecular vibrational modes (Figure 1B). Both ERS and VRS signals undergo enhancement by a factor of $|E_{SP}|^4/|E_0|^4$ in plasmonic nanocavity hotspots, where E_{SP} is the local plasmonic electrical field and E_0 is the electrical field of incident excitation light.[47] During in situ EC-SERS measurements (Figure 1C), PE-ERS and PE-VRS signals, originating from electronic states and molecular vibrational bonds at electrode/electrolyte interfaces, respectively, within the plasmonic hotspots can provide complementary insights into interfacial electrochemical activities during redox reactions.

The NLNOEs, depicted in Figure 1C, support an electrical dipole (ED) plasmon mode, concentrating enhanced electric fields at nanocavities' upper edges and consequently facilitating the generation of PE-ERS and PE-VRS signals with a shared plasmonic enhancement factor (EF).[48] Through electric potential modulation using a potentiostat, NLNOEs enable comprehensive EC-SERS spectral data collection, encompassing PE-ERS and PE-VRS signals. The NLNOE substrate functions as the working electrode (WE) in our in situ EC-SERS setup,[46,54] connected to the potentiostat via a copper wire, while a saturated Ag/AgCl electrode and a platinum wire acts as the reference (RE) and counter electrodes (CE), respectively. To optimize the observation of PE-ERS signals and minimize interference from photoluminescence generated by interband transitions in the gold and silver layers, a 785 nm near-infrared CW laser is employed for excitation. This EC-SERS configuration permits multiple cyclic voltammetry (CV) runs, capturing a temporally evolving EC-SERS spectrum.

Efficient signal collection in spectroelectrochemical techniques necessitates hotspots that are electrochemically active, electrically connected, and possess high plasmonic EFs. To achieve this, we designed two-tier Au-Ag NLNOEs with alternating gold and silver layers (Figure 1C). Our prior work[46,54] established the foundation for this approach. Here, we utilize a scalable nanoimprinting fabrication process (Figure 1D) to produce wafer-scale NLNOE substrates specifically tailored for in

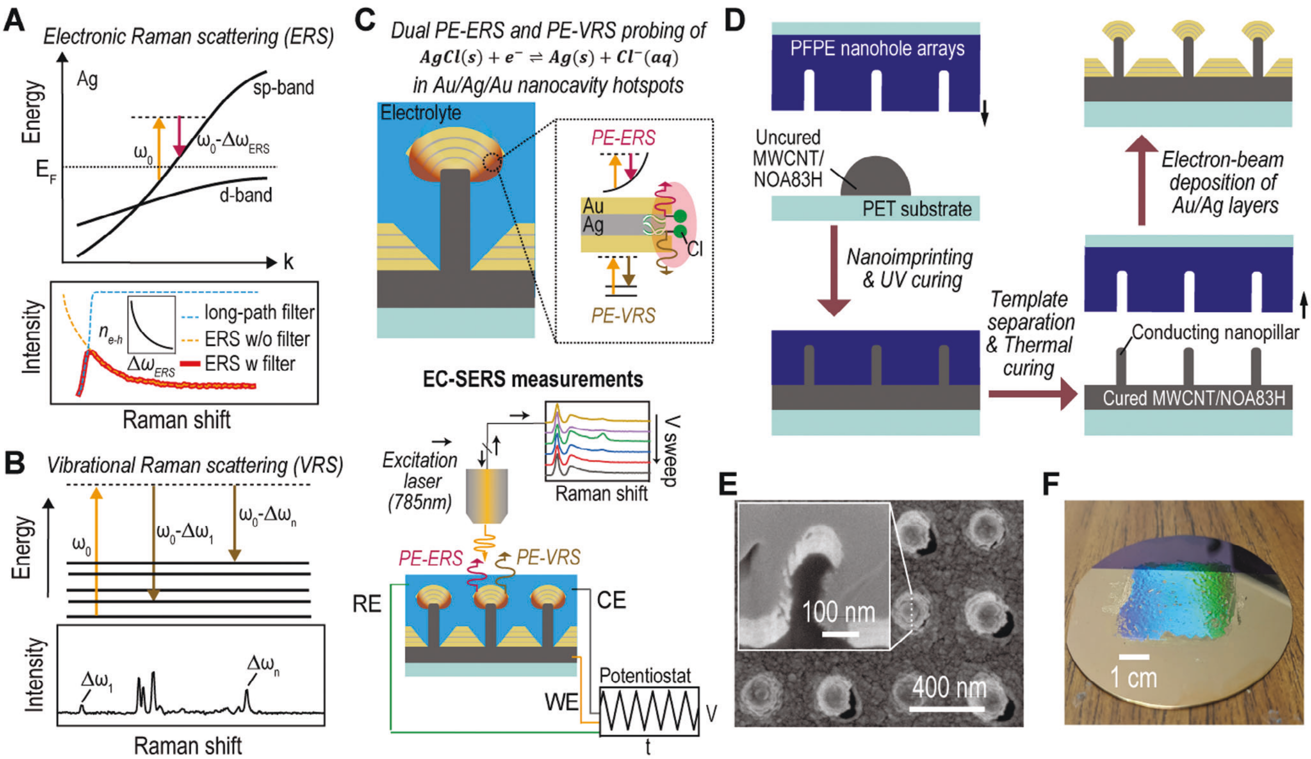

Figure 1. Overview of Plasmon-Enhanced Raman Scattering Processes and Nanolaminate Nano-Optoelectrode Devices. A) Illustration of electronic Raman scattering (ERS) in a metal sp-band near the Fermi energy level, E_F. B) Schematic representation of vibrational Raman scattering (VRS). C) Top: Depiction of both plasmon-enhanced electronic Raman scattering (PE-ERS) and plasmon-enhanced vibrational Raman scattering (PE-VRS) in the hotspots of nanolaminate nano-optoelectrodes (NLNOEs) composed of alternating nanoscale layers of Au and Ag. Bottom: Schematic of in situ electrochemical surface-enhanced Raman spectroscopy (EC-SERS) measurements employing Au/Ag NLNOEs during cyclic voltammetry (CV). D) Sequential steps outlining the fabrication process of Au/Ag NLNOEs. E) Scanning electron microscopy (SEM) top-view image of NLNOEs. Inset: Cross-sectional SEM image obtained through focused ion beam (FIB) milling. F) Optical image displaying NLNOEs on a three-inch silicon wafer substrate, demonstrating the uniformity and scalability of the nanoimprinting-based fabrication process.

situ EC-SERS measurements. The fabrication process begins with a reusable inverse template of perfluoropolyether (PFPE) nanohole arrays on a polyethylene terephthalate (PET) substrate. PFPE's low surface energy and high Young's modulus make it ideal for repeated use. This template is created from a silicon master of square pillar arrays via nanoimprint lithography. We then mold the template using a multiwall carbon nanotube (MWCNT, a mass fraction of 20%) doped commercial UV light-curable polyurethane (PU, NOA83H) compound, yielding conductive MWCNT/PU nanopillar arrays on Si substrates.[54] Next, alternating layers of Au (≈25 nm) and Ag (≈8, ≈10, and ≈12 nm from bottom to top) are deposited onto the nanopillar arrays via electron-beam evaporation, creating Au/Ag NLNOE arrays. The thicker gold layers (≈25 nm) compared to the silver layers (≈8, ≈10, and ≈12 nm) in our nanolaminate design serve two primary purposes: ensuring robustness by protecting the reactive silver during electrochemical processes, and promoting the hybridization of plasmonic electric dipole and magnetic dipole modes in the visible-NIR range for enhanced near-field intensity and strong SERS signals, as demonstrated in our previous studies[55,56] A brief wet etching (1 min) of Ag using Cr etchant forms nanocavities, exposing plasmonic Au-Ag-Au nanocavity hotspots to the electrolyte, crucial for $AgCl(s) + e^- \rightleftharpoons Ag(s) + Cl^-(aq)$ redox reactions. While AgCl redox reactions can change surface roughness,[57] this effect is generally less critical for plasmonic enhancement than intense gap plasmonic modes. Figure 1E shows a focused ion beam (FIB) milled cross-section of the NLNOE sample obtained using scanning electron microscopy (SEM). Figure 1F demonstrates the scalability of the process with the wafer-scale NLNOE sample exhibiting homogenous light diffraction, indicating large-area uniformity in the periodic nanostructures.

To assess the suitability of NLNOEs for in situ EC-SERS, we conducted a thorough investigation of their optical and electrochemical properties. We used a visible-to-near-infrared (vis-NIR) spectrophotometer to perform reflectance spectroscopy on a ≈2 cm^2 NLNOE sample. **Figure 2A** compares the measured reflectance spectra with finite-difference time-domain (FDTD) simulations in the 400 to 1000 nm wavelength range. The measured reflectance spectrum displays a broad reflective dip (≈20%) from 400 nm to 500 nm attributed to gold interband transitions. Reflectance increases to ~80% between 500 nm and 700 nm due to higher linear backscattering. Our FDTD simulations, qualitatively aligning with the measurements, reveal an electric dipole mode at ≈720 nm. This mode corresponds to localized field enhancement at the upper rim of the nanocavity (see the X-Z cross-section of near fields $|E|^2$ in Figure 2A). Minor discrepancies in the spectra (e.g., dips at ≈550 nm and ≈720 nm in simulations)

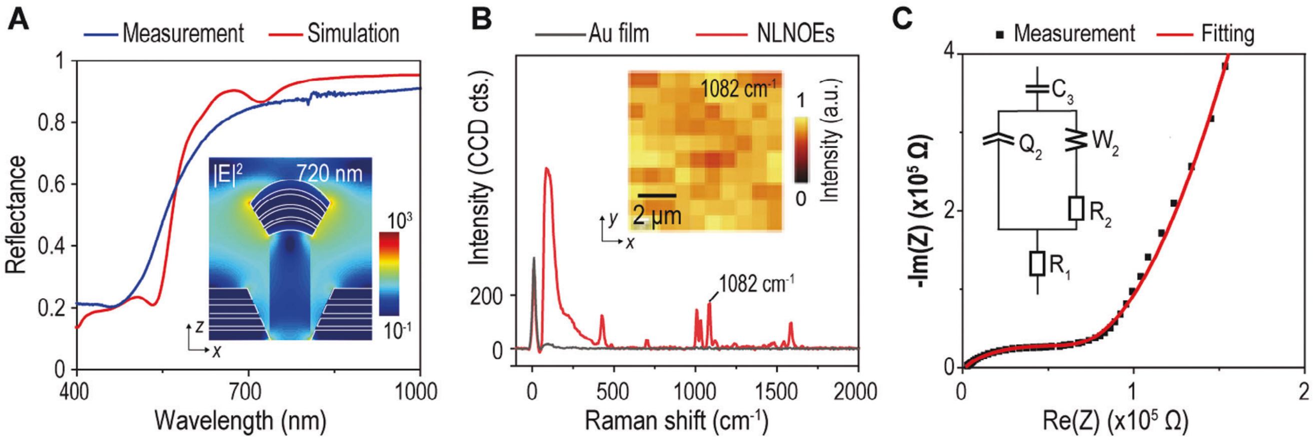

Figure 2. Analysis of Plasmonic and Electrochemical Interfacial Properties of NLNOEs. A) Comparative reflectance spectra derived from both FDTD simulations and direct measurements, spanning 400 nm to 1000 nm wavelengths. Inset: x-z cross-section of the electric field intensity $|E|^2$ at 720 nm, with white lines representing Au boundaries. The FDTD simulation uses a plane wave source with x-polarization and z-traveling direction. B) PE-VRS enhancement factor (EF) characterization using benzenethiol (BZT) molecules on both flat Au film and NLNOEs coated with a monolayer of BZT. SERS measurements cover an 8×8 µm^2 area, with integration times set at 100 s for flat Au and 0.5 s for NLNOEs. Inset: Spatial distribution of the PE-VRS peak at 1082 cm^{-1} from BZT on NLNOEs. C) Electrochemical impedance spectroscopy (EIS) results for NLNOEs and the corresponding equivalent circuit model with parameters obtained from fitting. Further details on EIS measurements and analysis are provided in the Supporting Information.

can be attributed to plasmonic mode broadening due to variations in the fabrication process.

To further validate the simulation results, we compared the SERS spectra from NLNOEs and flat gold samples with surface-modified benzenethiol (BZT) monolayers (details in Supporting Information). Figure 2B displays the comparative analysis of averaged spectra of BZT on planar gold and NLNOEs from area scans. While flat gold yielded no discernible BZT peaks, the NLNOEs significantly amplified the signature peaks due to plasmonic enhancement. We calculated an estimated SERS EFs of ≈10^6 for NLNOEs under 785 nm laser excitation with the formula: SERS EF $= (I_{\mathrm{SERS}}/N_{\mathrm{SERS}})/(I_{\mathrm{Raman}}/N_{\mathrm{Raman}})$, where I_{SERS}, I_{Raman}, N_{SERS}, and N_{Raman} are the BZT SERS intensity, neat BZT Raman intensity, and the numbers of BZT molecules contributing to BZT SERS and neat BZT Raman intensities, respectively.[58]

Electrochemical impedance spectroscopy (EIS) was performed on NLNOEs immersed in 1× Phosphate-Buffered Saline (PBS) solution (pH 7.4) at ambient temperature to study their electrical and electrochemical properties. The PBS solution was chosen to mimic the cellular environment. Figure 2C shows the Nyquist plot and the equivalent circuit fitting curve (see Supporting Information, Table S1 for detailed fitting results). Notably, the non-ideal capacitor Q_2 has a coefficient of order ($a_2 = 0.745$),[54,59] reflecting the nanostructured geometry of the NLNOE interface on top of the MWCNT/PU nanopillar arrays.

To precisely control the redox reaction within the Ag nanogap cavities, we performed cyclic voltammetry within a potential window of 0.4 to −0.6 V. We used a low scan rate of 50 mV s^{-1} to induce the $AgCl(s) + e^- \rightleftharpoons Ag(s) + Cl^-(aq)$ redox reaction while maintaining the inertness of the Au layer.[60] **Figure 3A** (upper segment) shows the periodic current modulations resulting from the cyclic voltage sweeps. This behavior confirms both the reversible nature of Faradaic and non-Faradaic processes and the stability of the NLNOEs.

The lower segment of Figure 3A presents a time-resolved EC-SERS waterfall plot spanning six cycles (−50 to 1500 cm^{-1}). For a closer examination of spectral features, we isolated 2 × 6 spectra (−50 to 500 cm^{-1}) within a single redox cycle (100 to 140 s, the 3rd cycle), as shown in Figure 3B. We chose the 3rd cycle to ensure the stability of the redox reaction within the nanocavities under the laser spot (diameter = 2 µm). Our analysis revealed three key observations: i) Elastic Scattering Stability: The elastic scattering peak at 0 cm^{-1} remains constant throughout the redox reaction. ii) PE-ERS and PE-VRS Modulation: Both the PE-ERS pseudo-peak at ≈87 cm^{-1} and the PE-VRS peak at ≈258 cm^{-1} (associated with Ag-Cl bonds[57,61]) undergo substantial modulation during oxidation (+0.2 V) and reduction (−0.2 V). Notably, the PE-VRS peak maintains its spectral position throughout. iii) Asynchronous PE-VRS Behavior: The PE-VRS intensity exhibits a more pronounced increase during oxidation (+0.2 V) compared to reduction (−0.2 V).

Figure 3C highlights the intricate relationship between electrochemical modulations and the dynamic changes observed in EC-SERS spectral features. By examining the correlation between electrochemical current (I) and the normalized inelastic scattering intensities of PE-ERS, PE-VRS, and elastic scattering signals during voltage modulation, we uncover several critical insights. First, the well-defined Faradaic peaks (oxidation at ≈0.38 V, reduction at ≈−0.22 V) confirm the occurrence of $AgCl(s) + e^- \rightleftharpoons Ag(s) + Cl^-(aq)$ redox reaction.[60] The large peak-to-peak distance (≈0.6 V) compared to typical Ag/AgCl cyclic voltammetry (≈0.152 V),[62] even considering the Nernst effect due to low electrolyte concentration, suggests a quasi-reversible reaction.[8] This behavior can originate from the formation of nanoporous electrolyte networks within the Ag/AgCl matrices inside the Au-Ag-Au nanocavities. These networks hinder the mass transport of ions in the reaction, thus slowing down the electron transfer rate.[57] Second, The PE-VRS peak at ≈258 cm^{-1}, corresponding to Ag-Cl stretching vibrations,[57,61] displays asynchronous intensity modulation during the Faradaic region. Notably, the PE-VRS peak intensity precedes the peak voltage of the Faradaic current, pointing to the crucial role of $(AgCl)^*$ TSs. These TS

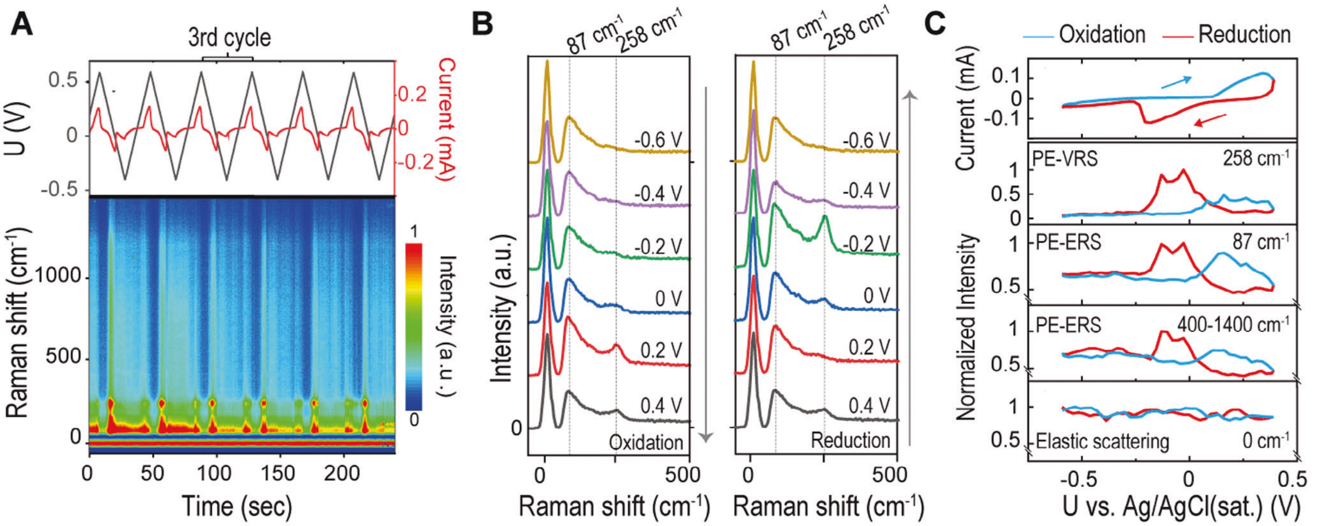

Figure 3. EC-SERS Measurement Insights of PE-ERS and PE-VRS Signals from Au/Ag NLNOEs under Electrode Potential Modulation during $AgCl(s) + e^- \rightleftharpoons Ag(s) + Cl^-(aq)$ redox cycles. A) Temporal current measurements (top) taken during CV from 0.4 to -0.6 V, alongside time-resolved EC-SERS spectra (bottom) under 785 nm laser excitation using NLNOEs in 1× PBS solution. B) EC-SERS emission spectra from NLNOEs in 1× PBS under 785 nm laser excitation at potentials ranging from 0.4 to -0.6 V during a single redox cycle, showcasing oxidation (left) and reduction (right) phases. C) Cyclic potential-dependent current (top) and normalized EC-SERS emission intensities (bottom) for critical spectral features: the PE-VRS peak at 258 cm^{-1} associated with the stretching vibration of Ag—Cl bonds, the PE-ERS pseudo-peak at 87 cm^{-1}, the broad continuum intensity of PE-ERS signals integrated from 400 to 1400 cm^{-1}, and elastic scattering peak at 0 cm^{-1}.

exhibit partial bonding, allowing greater vibrational degrees of freedom compared to the steady-state, polar covalent Ag—Cl bond. This increased freedom amplifies the VRS transition dipole moment, amplifying the PE-VRS signal. The short-lived nature of TS makes direct time-resolved optical observation of individual TSs challenging; however, plasmonic hotspots within our nanocavities significantly boost scattering events of ensemble TSs, enabling their ensemble detection. Furthermore, the contrasting electrical fields during oxidation and reduction can influence the orientation of the microscopic VRS dipole moment for (AgCl)* relative to the plasmonic field, leading to the observed intensity variations. Third, the voltage-dependent behavior of both the PE-ERS pseudo-peak (≈87 cm^{-1}) and the tail intensities (400–1400 cm^{-1}) suggests a common origin. Importantly, the PE-ERS pseudo-peak and the PE-VRS peak (≈258 cm^{-1}) exhibit a strong correlation in their voltage-dependent behavior, indicating that the generation of (AgCl)* TSs influences both PE-VRS and PE-ERS events. While PE-VRS intensity is modulated asymmetrically under oxidation and reduction, PE-ERS intensity changes remain consistent, suggesting that the ERS dipole moment orientation of (AgCl)* relative to the plasmonic field is unaffected by opposing electrical field directions. Finally, the elastic scattering peak (0 cm^{-1}) exhibits minor random fluctuations (≈10%). These could be attributed to plasmonic heating effects, which can induce local refractive index changes[63] or to the formation of vapor/gas nanobubbles.[64]

To explain the dynamic PE-ERS and PE-VRS variations observed in Figure 3, we propose a microscopic model illustrated in **Figure 4**. This model captures the evolution of these signals during the electrochemical redox processes. Figure 4A depicts the potential energy landscape as a function of the generalized coordinate (Ag-Cl interatomic distance) during $AgCl(s) + e^- \rightleftharpoons Ag(s) + Cl^-(aq)$ at the electrode/electrolyte interface. At the minimum energy configuration (r_0), strong coupling between Ag sp bands and Cl p orbitals forms hybridized Ag-Cl orbitals with a 3.3 eV energy gap.[65] This stable state corresponds to the steady-state Ag-Cl bond, which is polar covalent and possesses a low Raman scattering cross-section.

As the reaction progresses, the system transitions through an energy-maximized state (r_{TS}), representing the (AgCl)* transition state complex. These (AgCl)* transition states can be attributed to the formation of trap states at the Ag-solution interface, exhibiting a continuous energy distribution between bonding and antibonding orbitals and indicating a less stable electronic configuration. At this point, the coupling between Ag and Cl orbitals weakens, leading to negligible energy gaps between hybridized bonding and antibonding orbitals within (AgCl)*, contributing to the observed extra PE-ERS signals. Our hypothesis regarding the (AgCl)* transition state electronic structure aligns with ab initio calculations,[7] where a possible transition state is described as a cluster at the interface exhibiting a continuous half-filled energy band. Notably, the synchronous modulation of PE-ERS with PE-VRS during the redox process supports the critical role of TSs with additional continuous energy states in explaining both signals. These considerations exclude alternative explanations involving intermediate states with significant energy gaps.

Furthermore, the enhanced electron cloud distortion within (AgCl)* leads to increased polarizability changes and a higher VRS transition dipole moment ($|\mu^*|$) compared to the steady-state Ag—Cl bond. Such increased polarizability translates to amplified PE-VRS signals. This premise, where the (AgCl)* TS features filled bonding and unoccupied antibonding orbitals with negligible energy gaps and a larger VRS transition dipole moment, serves as the foundation for our subsequent analysis of modulated PE-VRS and PE-ERS signals in the Faradaic process.

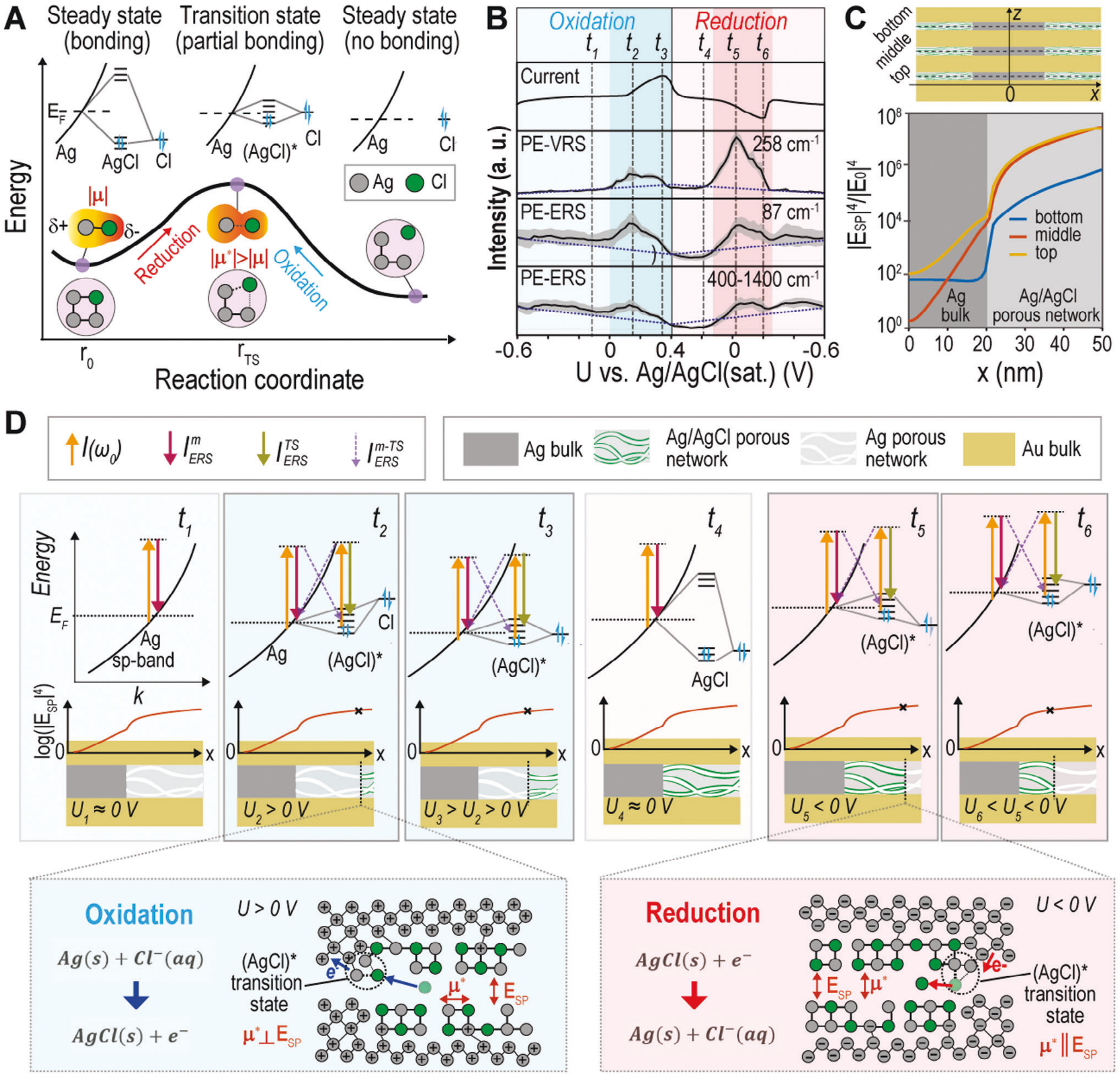

Figure 4. Correlated Monitoring of Transition States in Electrochemical Redox Reactions Using PE-ERS and PE-VRS. A) Diagram illustrating the interfacial electronic and vibrational structures linked to Ag—Cl bond dynamics during the $AgCl(s) + e^- \rightleftharpoons Ag(s) + Cl^-(aq)$ electrochemical redox reaction within Au/Ag/Au nanogap hotspots at the electrode-electrolyte interface. B) Time-dependent, voltage-resolved representation of measured electrical current, PE-VRS, and PE-ERS intensities. The plots present average signals with shaded regions indicating standard deviation (± SD) over five cycles at different voltages ($n = 5$, the electrical current standard deviation is not shown due to <1% variation). Blue and red shadings highlight the oxidation (potential increase) and reduction (potential decrease) phases, respectively. The labels t_1 to t_6 mark six characteristic times within one redox cycle. The dashed line beneath the PE-ERS and PE-VRS signal curves represents non-Faradaic voltage modulation-induced contributions. C) FDTD-estimated near-field enhancement factor $|E_{SP}|^4/|E_0|^4$ as a function of x position for PE-ERS and PE-VRS emissions within the Au-Ag-Au nanogap containing Ag/AgCl nanoporous networks. D) Microscopic illustration of changes between the steady-state covalent Ag—Cl bonds (or Ag and Cl elements) and the $(AgCl)^*$ transition state (TS) within the nanoporous Ag/AgCl network at six representative times (t_1 to t_6) corresponding to Figure 4B.

Figure 4B highlights a crucial finding: a temporal discrepancy exists between the peaks and turn-on/turn-off phases of the electrochemical current and the PE-VRS/PE-ERS emission intensities. This observation, coupled with insights from Figure 3C, suggests that the behaviors of PE-ERS and PE-VRS signals are influenced by the spatial locations where $(AgCl)^*$ TSs emerge within the plasmonic nanocavities. Meanwhile, it should be noted that the PE-ERS signal in the high wavenumber range (400–1400 cm^{-1}) has a weaker Faradaic modulation compared to the low wavenumber range (87 cm^{-1}). This difference arises from energy constraints within the hybridized electronic states of the transition state complex, which can limit the allowed electronic transitions in the high wavenumber range where the energy separation between initial and final states is larger. Figure 4C presents FDTD-estimated average enhancement factors (EFs), $|E_{SP}|^4/|E_0|^4$ in which E_{SP} represents the local electric fields at the wavelength = 720 nm where the surface plasmonic mode is in resonance for both PE-ERS and PE-VRS as a function of location (x) within the top, middle, and bottom Au-Ag-Au nanogap cavities of our NLNOE structure. It is important to note that we approximate the exact EF = $|E(\omega_L)|^2|E(\omega_R)|^2/|E_0|^4$, where $E(\omega_L)$ and $E(\omega_R)$ are local electric fields at the excitation laser frequency ω_L and Raman emission frequency ω_R. This approximation is valid since the plasmon resonance is sufficiently broad to encompass both the excitation and Raman emission wavelengths and $E(\omega_L)$, $E(\omega_R)$ and E_{SP} have nearly the same intensity. We approximate the complex Ag-AgCl nanoporous network using an idealized cylindrical NLNOE with random dielectric nanoparticles within the Ag layers. Notably, the enhancement factor exhibits a sharp decline as x decreases. This spatial decay of plasmonic field enhancement arises because the Ag/AgCl network effectively behaves as a nanoporous metal with reduced ohmic losses compared to pure Ag. The resulting metal-insulator-metal (MIM) configuration exhibits a characteristic decay of the enhancement factor away from the gap edges.

Figure 4D illustrates the interplay between electrochemical dynamics and signal evolution at six distinct times (t_1 to t_6, marked in Figure 4B) during oxidation and reduction. i) Pre-reaction (t_1 and t_4): Before oxidation or reduction begins, PE-ERS is modulated by capacitive charging/discharging of the metal surface. In the absence of TSs, PE-VRS remains unaffected. ii) Reaction Onset (t_2 and t_5): When $AgCl(s) + e^- \rightleftharpoons Ag(s) + Cl^-(aq)$ redox reaction initiates, Faradaic current increases, and PE-ERS/PE-VRS peaks occur due to TS formation. iii) Peak Current with Declining PE-ERS/PE-VRS Signal (t_3 and t_6): While Faradaic current reaches its maximum, PE-ERS and PE-VRS intensities begin to decrease.

Understanding how $(AgCl)^*$ transition states (TS) contribute to the emission intensity of the PE-ERS signal is crucial. These TSs involve the hybridization of Ag sp bands near the Fermi level with Cl atomic orbitals, leading to continuous energy states. These new states offer additional pathways for electron transition and relaxation, thereby enhancing PE-ERS intensity. To systematically analyze the contributions of different electron transition pathways to the total PE-ERS intensity, $I_{ERS}(\delta\omega, r, \Delta)$, we can introduce the following equation:

$$I_{ERS}\ (\delta\omega, r, \Delta) = I_{ERS}^{m}\ (\delta\omega, r) + I_{ERS}^{TS}\,(\delta\omega, r, \Delta) + I_{ERS}^{m-TS}\,(\delta\omega, r, \Delta) \quad (1)$$

This equation categorizes PE-ERS processes into three groups based on their electronic transition pathways. i) $I_{ERS}^{m}\ (\delta\omega, r) = f_{SP}\ (\delta\omega, r) Q_m \int_0^\infty g_m(E) f_T(E) g_m(E + \hbar\delta\omega)[1 - f_T(E)]dE$: This term represents PE-ERS processes occurring solely within the Ag sp band. It depends on the PE-ERS enhancement factor (EF), $f_{SP}(\delta\omega,r) \approx |E_{SP}(\delta\omega,r)|^4/|E_0|^4$, at the shifted frequency ($\delta\omega$) and position (r). The integral incorporates the electronic density of states for the metal (Ag) sp-band at energy E, denoted by $g_m(E)$. The Fermi-Dirac distribution ($f_T(E)$) accounts for electron occupation probabilities at each energy level. Q_m is the corresponding ERS cross-section constant in metal. ii) $I_{ERS}^{TS}\ (\delta\omega, r, \Delta) = f_{SP}\ (\delta\omega, r) Q_{TS} \int_0^\infty g_{TS}^{\Delta}(E) f_T(E) g_{TS}^{\Delta}(E + \hbar\delta\omega)[1 - f_T(E)]dE$: This term represents PE-ERS processes involving transitions mediated by both initial and final states residing within the hybridized $(AgCl)^*$ TSs. It incorporates the electronic density of states for the TSs with an energy bandgap of Δ and centered at energy E, denoted by $g_{TS}^{\Delta}(E)$. Q_{TS} is the corresponding ERS cross-section constant for TSs. iii) $I_{ERS}^{m-TS}\ (\delta\omega, r, \Delta) = f_{SP}\ (\delta\omega, r)\{Q_{TS\rightarrow m} \int_0^\infty g_{TS}^{\Delta}(E) f_T(E) g_m(E + \hbar\delta\omega)[1 - f_T(E)]dE + Q_{m\rightarrow TS} \int_0^\infty g_m(E) f_T(E) g_{TS}^{\Delta}(E + \hbar\delta\omega)[1 - f_T(E)]dE\}$: This term represents PE-ERS processes involving transitions where only one of the initial or final states resides within the $(AgCl)^*$ TSs. They utilize g_{TS}^{Δ}(E) for the TS electronic density of states with an energy bandgap (Δ) and centered energy (E). $Q_{TS\rightarrow m}$ and $Q_{m\rightarrow TS}$ are the respective ERS cross-section constants.

Notably, I_{ERS}^{m} is solely influenced by non-Faradaic capacitive charging/discharging and is independent of the Faradaic redox process. In contrast, I_{ERS}^{TS} and I_{ERS}^{m-TS} can increase due to the formation of hybridized $(AgCl)^*$ TSs with continuous energy levels. These TSs provide an additional density of states through the atom's p orbitals. When a steady-state covalent Ag—Cl bond forms, strong interatomic hybridization creates bonding and antibonding states with a large energy gap, eliminating their contribution to PE-ERS signals. Therefore, the additional PE-ERS terms (I_{ERS}^{TS} and I_{ERS}^{m-TS}) only appear during the Faradaic redox process when $(AgCl)^*$ TSs are formed, depicted in the top row of Figure 4D, where the transition pathways contributing to PE-ERS (I_{ERS}^{m}, I_{ERS}^{TS} and I_{ERS}^{m-TS}) are color-coded.

Like PE-ERS, PE-VRS also arises only in the presence of $(AgCl)^*$ TSs. The weakly coupled electrons in these TSs have an enhanced capacity for electron cloud distortion compared to the polar covalent Ag—Cl bond in the steady state. This distortion leads to more significant VRS transition dipole moments ($|\mu^*|$), resulting in stronger PE-VRS signals. Consequently, PE-VRS follows PE-ERS trends with the emergence of $(AgCl)^*$ TSs during the redox reaction.

However, PE-VRS exhibits a distinct feature: a difference in the amplitude of Faradaic modulation for oxidation and reduction. This variation may arise from the varying average orientations of the $(AgCl)^*$ TSs due to the attractive or repulsive electrostatic forces exerted by the positive or negative metal electrode voltages, respectively. As illustrated in the bottom plots of Figure 4D, the $(AgCl)^*$ TSs appear at the boundary of Ag-AgCl porous network channels with different orientations due to the polarity change of induced charges on the metal surface. These different orientations lead to varying alignments of the VRS dipole moment (μ^*) with the plasmon-driven electric field (E_{SP}) in hotspots. As a result, the Faradaic modulation amplitude is more pronounced during reduction than oxidation. While the formation of the $(AgCl)^*$ transition state involves modifications in the Ag—Cl bond, these changes do not induce a significant shift in the vibrational frequency; the modifications primarily affect the bond's polarizability, influencing the PE-VRS intensity, rather than causing a noticeable change in the peak position.

While the formation of AgCl* transition states contributes to the observed spectral changes, it is important to consider the potential influence of any variations in the NLNOE nanostructure during the oxidation-reduction cycle. However, as demonstrated in our previous work[46] and as shown in Figure S3 in Supporting Information, the electrochemical processes do not induce significant modifications to the NLNOE geometry. Moreover, the dominance of the emissions tied to the gap modes in our NLNOE-based SERS platform, with their strong field enhancements, outweighs the influence of any minor morphological changes on the SERS signal.

The plasmonic amplification of both PE-ERS and PE-VRS signals is proportional to $|E_{SP}|^4/|E_0|^4$. As depicted in Figure 4C, $|E_{SP}|^4/|E_0|^4$ decays exponentially along the nanoporous Ag/AgCl networks formed within the Au-Ag-Ag nanocavities during the redox reaction. This spatial decay of plasmonic field enhancement arises because the Ag/AgCl network effectively behaves as a nanoporous metal but exhibits reduced ohmic losses compared to pure Ag. During oxidation/reduction reactions, the generated $(AgCl)^*$ TSs migrate inward within the nanoporous network (middle row, Figure 4D). This inward migration, driven by the electrochemical reaction, leads to progressively weaker field enhancements for both PE-ERS and PE-VRS signals. Consequently, the peak intensities of PE-ERS and PE-VRS signals deviate from the Faradaic current profile (Figure 4B) due to the combined effects of TS generation and their dynamic spatial redistribution within the nanocavities, which modulates the local electric field intensity experienced by TSs.

We have previously discussed the effect of non-Faradaic modulation on PE-ERS and PE-VRS in depth.[46] It is important to reiterate that surface charge modulation within the Debye length of the electrode surface causes a shift in the Fermi energy level on the Ag surface (top row, Figure 4D). This effect leads to a linear, voltage-dependent decline in the PE-ERS signal intensity from metal hotspots, $I^{m}_{ERS}(\delta\omega, r)$. Since this charge modulation overlaps with the decay length of the plasmonic field, the resulting PE-ERS signals are highly sensitive to both Faradaic and non-Faradaic variations in voltage.

To further explore the broader applicability of our dual-channel EC-SERS methodology, we investigated its performance with Au-sidewall-coated Au-Ag-Au NLNOE devices immersed in a mixed electrolyte of PBS and KH_2PO_4. These NLNOE devices,[46] fabricated on pure PU nanopillar arrays with an additional Au sidewall coating for electrical conductivity, retain the same Au/Ag/Au layer structure as the NLNOEs used in the previous experiment. The fabrication details of the Au-sidewall-coated Au-Ag-Au NLNOEs are provided in the Supporting Information.

We investigated the Au-sidewall-coated Au-Ag-Au NLNOE devices in solutions with varying proportions of 1× PBS and 1× PBS-equivalent KH_2PO_4 (152 mMol/L) to maintain a constant total ion concentration while altering the Cl^- concentration. This mixed electrolyte approach allows us to systematically modulate the availability of Cl^- ions and selectively promote different redox reactions involving silver, specifically Ag/AgCl or Ag/AgH_2PO_4 while maintaining a constant total ionic strength. **Figure** 5A displays the cyclic voltammograms for varying proportions of 1× PBS and 1× PBS-equivalent KH_2PO_4 (152 mMol L^{-1}). The non-Faradaic current remains constant due to the fixed total ion concentration. However, multiple Faradaic peaks suggest the occurrence of multiple electrochemical reactions. i) Silver Oxide Redox: Broad Faradaic peaks near 0.2 V, with amplitudes increasing with higher Cl- concentration (PBS proportion), are attributed to the redox reaction of silver oxides at the NLNOE surface. ii) Ag/AgCl and Ag/AgH_2PO_4 Redox: Narrower pairs of peaks between −0.05 and 0.2 V correspond to redox reactions between Ag and $Cl^{-}/KH_2PO_4{}^{-}$ ions. A single oxidation peak suggests that both AgCl and AgH_2PO_4 share an oxidation process where Ag is converted to Ag^+. However, two distinct reduction peaks with varying intensities as a function of Cl- concentration indicate separate reduction pathways for AgCl and AgH_2PO_4. Specifically, the peak at the increased positive voltage is due to the reduction of AgCl and the peak at the decreased negative potential is due to the reduction of AgH_2PO_4. Such closed reduction voltages agree with the cyclic voltammetry results from the previous work.[66] It should be noted that between Figures 3 and 5, the Faradaic voltage peak-to-peak separation is different under 1× PBS solution. Such difference is influenced by the ohmic resistance of the NLNOE, which can vary depending on the specific nano-geometries and nanostructures at plasmonic nanocavity hotspots. However, the quasi-reversible nature of the Ag/AgCl redox reaction does not affect the core findings of this study. On the contrary, the measurements with different NLNOEs present the tendencies of PE-ERS and PE-VRS which follow the principles we have established previously in this work. Such consistency proves the universality and credibility of our theory.

Figure 5B illustrates the voltage modulation of PE-ERS and PE-VRS under low and high Cl- concentrations. These plots present average intensity curves at specific voltages over complete cycles, with error bars representing standard deviations. There are several key observations. i) At low Cl^- concentration (KH_2PO_4:PBS = 10:1), only non-Faradaic linear modulations are observed on AgCl PE-VRS and PE-ERS intensities. ii) At higher Cl^- concentration (KH_2PO_4:PBS = 1:10 & 1:1), both Faradaic (≈0 V) and non-Faradaic modulations exist. Higher Cl^- concentration leads to higher Faradaic PE-ERS and PE-VRS modulations and voltage shifts consistent with CV plots. iii) AgCl transition states support PE-VRS peak at 258 cm^{-1}, while AgH_2PO_4 does not. iv) Linear PE-ERS non-Faradaic modulation is consistent with Figure 4B. The modulation depths of non-Faradaic modulations remain constant across all Cl^- concentrations due to unchanged total ion concentrations.

To gain deeper insights into the interplay between the Ag/AgCl and Ag/AgH_2PO_4 redox reactions and their influence on the plasmonic response, we analyzed the normalized modulation depths of the PE-ERS and PE-VRS signals. These modulation depths were statistically derived from each set of EC-SERS measurements, as shown in Figure 5C. (Details of the calculation are provided in the Supporting Information.) We observe that significant Faradaic modulations on both PE-ERS and PE-VRS signals occur predominantly when the Cl^- concentration is high (KH_2PO_4:PBS ≤ 1:1). This observation suggests the crucial role of the Ag/AgCl redox reaction in generating these modulations. In contrast, the normalized non-Faradaic modulation remains consistent across all experimental conditions. This consistency is attributed to the unchanged total ion concentration and electric double-layer capacitance, which are the primary factors governing the non-Faradaic response.

To further elucidate the observed trends, we propose a mechanistic interpretation illustrated in Figure 5D. This schematic depicts the competition between the Ag/AgCl and Ag/AgH_2PO_4

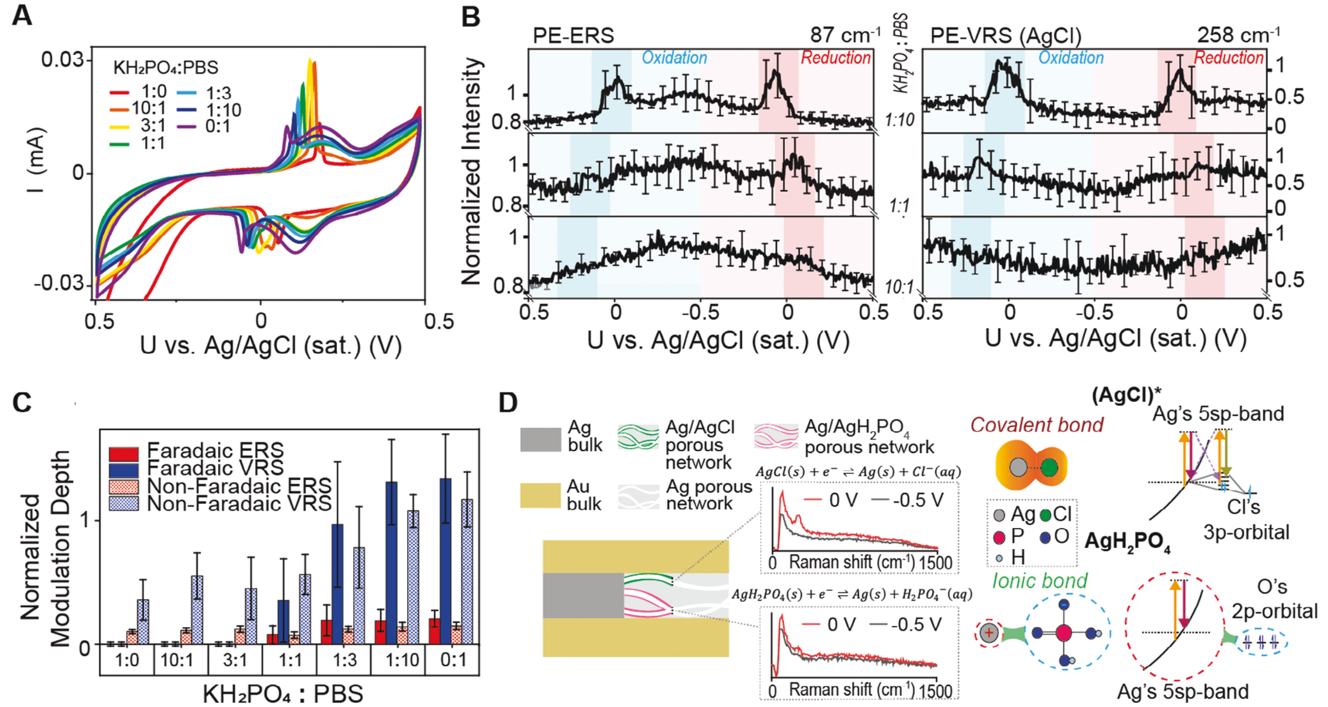

Figure 5. Modulating Electrochemical Reactions and PE-VRS/PE-ERS Responses in Mixed 1× PBS/KH_2PO_4 Solutions. A) Cyclic voltammograms obtained in solutions with varying volume ratios of 1× PBS and 1× PBS-equivalent KH_2PO_4 portions (152 mMol L^{-1}). Each voltammogram represents the average of 10 cycles. B) Potential-dependent PE-ERS (87 cm^{-1}) and PE-VRS (258 cm^{-1} for Ag—Cl bond) intensities recorded during cyclic voltammetry in the mixed solutions. The curves represent averages over a total 10 cycles ($n = 10$), with error bars indicating the standard deviation (± SD) at 20 uniformly selected voltages. C) Normalized modulation depths of PE-ERS and PE-VRS signals as a function of 1× PBS/KH_2PO_4 ratio, separated into Faradaic and non-Faradaic contributions. Faradaic modulation depth is calculated by subtracting the peak intensity from the linear non-Faradaic background in both anodic and cathodic directions and normalizing by the non-Faradaic background intensity at the peak potential. Non-Faradaic modulation depth is determined by the intensity difference between 0.5 and 0 V, normalized by the intensity at 0 V. Details of the modulation depth calculation are provided in the Supporting Information. The result modulation depths are represented as averages with error bars of standard deviations (± SD) from a total of 10 cycles ($n = 10$). D) Schematic illustration of the distinct PE-VRS/PE-ERS responses and electronic structures of AgCl and AgH_2PO_4 formed during the Faradaic processes. The spectrum represents the difference in optical response between pure 1× PBS and pure KH_2PO_4 solutions (152 mMol L^{-1}) during the oxidation process (0 to 0.5 V).

redox reactions within the Ag nanolayers in Au-Ag-Au NLNOE devices. First, the finite number of reaction sites within the porous Ag network are occupied by either Ag/AgCl or Ag/AgH_2PO_4, as both reactions involve the formation of solid layers via oxidation within the porous layers. Second, only the AgCl transition states provide additional PE-ERS and PE-VRS signals during the Faradaic reactions. This selectivity is supported by the spectral comparison at 0 V between pure PBS and pure KH_2PO_4 solutions (shown in the middle panel of Figure 5D). Third, during the redox reaction, AgH_2PO_4 possesses predominantly ionic bonds. Such ionic bonds at the Ag/AgH_2PO_4 interface do not support strong surface-enhanced Raman signal as previous work has presented.[65] Furthermore, the ionic bonds also do not support the continuous interfacial hybridized states to support the additional ERS pathway, as depicted in the right panel of Figure 5D. In contrast, the AgCl transition state, with its more covalent character, can result in both PE-ERS and VRS signal enhancements. Notably, this proposed mechanism explains the absence of significant Faradaic modulation for PE-ERS and PE-VRS when the Cl^- concentration is low (KH_2PO_4:PBS > 1:1). Under these conditions, the limited availability of reaction sites for Ag/AgCl formation restricts the generation of detectable signals above the noise level.

The dual-channel EC-SERS measurements conducted with different NLNOEs, and chemical environments demonstrate the universality of the PE-ERS and PE-VRS signal analysis for Faradaic processes. This approach enables tracking and analyzing the ensemble electronic structure of electrochemical interfaces during Faradaic processes, going beyond traditional EC-SERS methodologies that primarily focus on vibrational fingerprints. The ability to detect electronic information for short-lived transition states from ensemble optical responses of redox reaction events offers new dimensions of information for interfacial chemical reactions, opening opportunities in the study of interfacial catalysis and biological sensing.

3. Conclusion

In summary, we have introduced a pioneering dual-channel EC-SERS methodology that synergistically combines PE-ERS and PE-VRS to capture both vibrational and electronic Raman information, providing unprecedented insights into interfacial transition state activities. This approach allows us to successfully probe the (AgCl)* TS activities during redox reactions within the plasmonic nanocavities of Au/Ag NLNOEs. By simultaneously monitoring both electronic and vibrational transitions, this dual-signal strategy offers a richer understanding of interfacial electronic states and significantly expands the scope of EC-SERS applications. Our novel NLNOE design strategically aligns electrochemical reaction sites with plasmonic nanogap hotspots, enabling efficient and accurate spectral measurements for reaction monitoring. The inherent versatility of the NLNOE platform, including the possibility of substituting the silver layer with other reactive materials, opens avenues for extensive exploration of various electrochemical reactions. The effectiveness of this method is demonstrated across different NLNOE nanostructures and chemical environments. Furthermore, our dual-channel EC-SERS methodology can distinguish different interfacial redox reactions based on the distinct electronic states associated with covalent bond and ionic bond characteristics, making it widely applicable for studying interfacial redox reactions in diverse electrochemical systems. While further research is needed to refine control over electrochemical interfacial properties and optimize nano-optoelectrode sensitivity, this work establishes a solid foundation for advancing EC-SERS methodologies. Our approach enables real-time, in situ observations of diverse electrochemical and electrocatalytic processes at electrode interfaces, holding enormous potential for significant advancements in fields ranging from electrocatalysis to biological sensing.

4. Experimental Section

Cr etching: After the fabrication of the NLNOE, a Cr etching was applied to the NLNOE to open the Ag layer gaps and add roughness to the NLNOE's sides. The etching process was performed under room temperature and the Cr etchant (CHROMIUM ETCHANT 1020, Transene Company, Inc.) was diluted with deionized water (etchant: water = 1: 50). The NLNOE was immersed in the diluted etchant in 1 min and immersed in deionized water twice and isopropyl alcohol once (each immersion took 2 min), sequentially. After all the immersion, the NLNOE was dried by an air blower.

Reflection measurements: The reflectance spectra of the samples were obtained using a UV–vis–near-infrared (NIR) spectrophotometer (Cary 5000), with a wavelength range extending from 400 to 1000 nm at intervals of 0.5 nm. At 830 nm, the detector was switched thus it provided a stitching error in the measured spectrum.

Numerical FDTD simulations: The 3D FDTD simulations were acquired using commercial software (FDTD solutions, Ansys-Lumerical Inc.) to numerically calculate the far-field spectra and the near-field distributions of the plasmonic systems. Optical constants of Au and Ag were taken from Johnson and Christy[67] in the spectrum range from 400 to 1000 nm. For the refractive index of MWCNT doped PU, a flat sample was fabricated with ≈1 µm polymer thickness on glass and ellipsometry to obtain the refractive index of MWCNT doped PU as $n = 1.54 + 0.05i$. To mimic the geometry of the sample according to the SEM and FIB images, the 400 nm × 400 nm square lattice was constructed with periodic boundary conditions in the x-y plane. For the nanopillar structure, a cone-shaped nanoparticle model and an angled gap surrounding the MWCNT doped PU pillar and the nanowell is adapted to mimic the shadowing effect in the deposition. The mesh size is 1 nm in the x, y, and z directions.

Electrochemical Measurements: A custom-made EC cell mounted onto the sample was designed to contain the liquid and hold the Ag/AgCl reference electrode (saturated in KCl) and platinum coil counter electrode. The electrodes are all connected to a commercial potentiostat (SP-200, BioLogic), which provides the potential control and current probe. The electrolyte solution was a phosphate buffer saline (PBS) composed of 137 mMol L^{-1} NaCl, 2.7 mMol L^{-1} KCl, 10 mMol L^{-1} Na_2HPO_4, and 1.8 mMol L^{-1} KH_2PO_4, with deionized water utilized for dilution. The EC cell was filled with ≈2 mL of electrolyte solution, with all measurements conducted at ambient temperature. All cyclic voltammetry measurements were performed under the scan rate of 50 mV s^{-1} for the optimized temporal spectral resolution and signal-to-noise ratio of spectral and electrochemical signals. It should be noted that while the scan rate in cyclic voltammetry affects the temporal resolution of spectral acquisition and the peak-to-peak separation in the voltammograms due to the quasi-reversible nature of the Ag/AgCl and redox reaction, it does not alter the fundamental chemical reactions or the associated PE-VRS and PE-ERS spectral shifts. Measurements were performed within 10 min after introducing the liquid to avoid electrolyte purging issues over a prolonged experiment (hours). The substrate was intermittently rinsed with the corresponding concentration of PBS solution to ensure its cleanliness and the reliability of the measurements. The same experimental setup was applied for the electrochemical measurements in Figure 5, except for replacing the NLNOE sample and the electrolytes.

EC-SERS measurements: Laser excitation at a wavelength of 785 nm and power of 2 mW was used for the Raman measurements, focused with a 10× objective (NA = 0.25) lens in a commercial confocal microscope (WITec alpha 300 SR System) in the backscattering configuration. The Raman spectroscopic microscope and potentiostat were controlled by separate computer workstations. Synchronization between the workstations was achieved through a network connection, enabling coordinated control of both instruments. The differing response times of the two instruments were calibrated to ensure accurate temporal alignment of the optical and electrochemical data. Single-point measurements were done at a 0.5 s integration time and captured by a CCD camera in a commercial spectrometer to measure the Stokes-Raman scattering. A long-pass filter was used to block elastically scattered light at the wavelength corresponding to the laser line (Rayleigh scattering), with the Stokes scattering transmitted through a multimode fiber (100 µm core diameter) wherein the cleaved fiber core functioned as the confocal pinhole. EC modulation was performed using a custom EC cell and commercial potentiostat, with the NLNOEs serving as the working electrode, a platinum coil as the counter electrode, and Ag/AgCl as the reference electrode, as previously described.

Statistical Analysis: During the in situ EC-SERS measurements the optical and electrochemical signals were collected with different interval times (optical: 0.5 s; electrochemical: 0.01 s). The spectrum-voltage relationship is then deducted from linear interpolation from spectrum-time and voltage-time relationships. Then the averaging is processed for further analysis among all the cycles performed (n = 5 for Figures 3 and 4, n = 10 for Figure 5), and the standard deviations are represented as the error bars (± SD). The data processing is achieved via OriginLab and MATLAB software.

Supporting Information

Supporting Information is available from the Wiley Online Library or from the author.

Acknowledgements

The authors gratefully acknowledge the support from the National Science Foundation (NSF) grant (DMR2139317), the Air Force Office of Scientific Research (AFOSR) grant (FA9550-23-1-0282), the Defense University Research Instrumentation Program (DURIP) Award (FA9550-19-1-0287), and the National Institute of Standards and Technology (NIST) grants (70NANB18H201 and 70NANB19H163).

Conflict of Interest

The authors declare no conflict of interest.

Author Contributions

Y.Z. and W.Z. conceptualized and ideated the project. W.Z. provided oversight for the project's execution. Y.Z. was responsible for conducting optical measurements, numerical simulations, and corresponding data analysis, under the guidance and assistance of W.Z. and E.M. Y.Z. and C.X. jointly conducted electrochemical measurements. The sample fabrication was a collaborative effort by Y.Z., C.X., and E.M. J.S. contributed to the structural characterization using FIB/SEM. W.Z., A.A., and H.L. participated in critical discussions and provided feedback on the manuscript. The manuscript was primarily authored by Y.Z. and W.Z. with substantial contributions from all team members. All authors have reviewed and approved the final manuscript.

Data Availability Statement

The data that support the findings of this study are available from the corresponding author upon reasonable request.

Keywords

electrochemical redox processes, electrochemical surface-enhanced Raman spectroscopy (EC-SERS), nanolaminate nano-optoelectrodes, plasmon-enhanced electronic Raman scattering (PE-ERS), plasmon-enhanced vibrational Raman scattering (PE-VRS)

Received: December 8, 2024
Revised: January 18, 2025
Published online:

---

[1] M. Dantus, M. J. Rosker, A. H. Zewail, *J. Chem. Phys.* **1987**, *87*, 2395.
[2] K. J. Laidler, *J. Chem. Educ.* **1988**, *65*, 540.
[3] Abidi, N., S. N. Steinmann, *Curr. Opin. Electrochem.* **2022**, 33.
[4] H. Chen, C. Jia, X. Zhu, C. Yang, X. Guo, J. F. Stoddart, *Nat. Rev. Mater.* **2023**, *8*, 165.
[5] P. Cheng, D. Zhong, A. H. Zewail, *J. Chem. Phys.* **1996**, *105*, 6216.
[6] T. L. Cocker, D. Peller, P. Yu, J. Repp, R. Huber, *Nature.* **2016**, *539*, 263.
[7] X. Ma, Y. Dai, M. Guo, Y. Zhu, B. Huang, *Phys. Chem. Chem. Phys.* **2013**, *15*, 8722.
[8] A. J. Bard, L. R. Faulkner, H. S. White, *Electrochemical methods: fundamentals and applications*, John Wiley & Sons, Hoboken **2022**, pp. 41–44.
[9] A. Vojvodic, J. K. Nørskov, *Natl. Sci. Rev.* **2015**, *2*, 140.
[10] W. F. DeGrado, *Nature.* **2003**, *423*, 132.
[11] X. Zhang, X. Cheng, Q. Zhang, *J. Energy Chem.* **2016**, *25*, 967.
[12] W. Kaim, J. Fiedler, *Chem. Soc. Rev.* **2009**, *38*, 3373.
[13] J. J. A. Lozeman, P. Führer, W. Olthuis, M. Odijk, *Analyst.* **2020**, *145*, 2482.
[14] Y. Zhai, Z. Zhu, S. Zhou, C. Zhu, S. Dong, *Nanoscale.* **2018**, *10*, 3089.
[15] K. Yue, W. Weipeng, M. Tian, Z. Ting, C. Junxian, Z. Zhengjun, *Front. Nanotechnol.* **2023**, 4.
[16] C. Y. Li, Z. Q. Tian, *Chem. Soc. Rev.* **2024**, *53*, 3579.
[17] J. M. Pitarke, V. M. Silkin, E. V. Chulkov, P. M. Echenique, *Rep. Prog. Phys.* **2007**, *70*, 1.
[18] A. Kinkhabwala, Z. Yu, S. Fan, Y. Avlasevich, K. Müllen, W. E. Moerner, *Nat. Photonics.* **2009**, *3*, 654.
[19] M. Kauranen, A. V. Zayats, *Nat. Photonics.* **2012**, *6*, 737.
[20] G. Sun, J. B. Khurgin, *Phys. Rev. A.* **2012**, 85.
[21] H. Aouani, M. Rahmani, M. Navarro-Cía, S. A. Maier, *Nat. Nanotechnol.* **2014**, *9*, 290.
[22] M. Celebrano, X. Wu, M. Baselli, S. Großmann, P. Biagioni, A. Locatelli, C. De Angelis, G. Cerullo, R. Osellame, B. Hecht, L. Duò, F. Ciccacci, M. Finazzi, *Nat. Nanotechnol.* **2015**, *10*, 412.
[23] M. Pelton, *Nat. Photonics.* **2015**, *9*, 427.
[24] S. A. S. Tali, R. R. H. H. Mudiyanselage, Y. Z. Qian, N. W. G. Smith, Y. M. Zhao, A. Morral, J. Y. Song, M. T. Nie, B. A. Magill, G. A. Khodaparast, *ACS Nano.* **2023**, *17*, 11362.
[25] S. A. S. Tali, W. Zhou, *Nanophotonics.* **2019**, *8*, 1199.
[26] M. T. Nie, Y. M. Zhao, W. Nam, J. Song, W. Q. Zhu, H. J. Lezec, A. Agrawal, W. Zhou, *Adv. Funct. Mater.* **2022**, *32*, 2202231.
[27] R. R. Frontiera, N. L. Gruenke, A. I. Henry, R. P. Duyne, *Abstr. Pap. Am. Chem. S.* **2012**, *243*.
[28] N. L. Gruenke, M. F. Cardinal, M. O. McAnally, R. R. Frontiera, G. C. Schatz, R. P. Van Duyne, *Chem. Soc. Rev.* **2016**, *45*, 2263.
[29] E. L. Keller, R. R. Frontiera, *ACS Photonics.* **2017**, *4*, 1033.
[30] D. Palecek, G. Tek, J. Lan, M. Iannuzzi, P. Hamm, *J. Phys. Chem. Lett.* **2018**, *9*, 1254.
[31] P. Kumar, H. Kuramochi, S. Takeuchi, T. Tahara, *J. Phys. Chem. Lett.* **2023**, *14*, 2845.
[32] N. C. Brandt, E. L. Keller, R. R. Frontiera, *J. Phys. Chem. Lett.* **2016**, *7*, 3179.
[33] L. D'Amario, M. B. Stella, T. Edvinsson, M. Persico, J. Messinger, H. Dau, *Chem. Sci.* **2022**, *13*, 10734.
[34] Q. Q. Lin, *Curr. Opin. Electrochem.* **2023**, 37.
[35] D. Wright, Q. Lin, D. Berta, T. Földes, A. Wagner, J. Griffiths, C. Readman, E. Rosta, E. Reisner, J. J. Baumberg, *Nat. Catal.* **2021**, *4*, 157.
[36] J. G. Wang, C. Jing, Y. T. Long, *Frontiers of Plasmon Enhanced Spectroscopy.* **2016**, *2*, 57.
[37] T. Isogai, K. Motobayashi, K. Ikeda, *J. Chem. Phys.* **2021**, *155*, 204702.
[38] K. A. Willets, *Curr. Opin. Electrochem.* **2019**, *13*, 18.
[39] G. Di Martino, V. A. Turek, A. Lombardi, I. Szabó, B. de Nijs, A. Kuhn, E. Rosta, J. J. Baumberg, *Nano Lett.* **2017**, *17*, 4840.
[40] T. Shegai, A. Vaskevich, I. Rubinstein, G. Haran, *J. Am. Chem. Soc.* **2009**, *131*, 14390.
[41] D. E.-Y. Wu, J. F. Li, B. Ren, Z. Q. Tian, *Chem. Soc. Rev.* **2008**, *37*, 1025.
[42] Z. Q. Tian, B. Ren, *Annu. Rev. Phys. Chem.* **2004**, *55*, 197.
[43] C. L. Brosseau, A. Colina, J. V. Perales-Rondon, A. J. Wilson, P. B. Joshi, B. Ren, X. Wang, *Nature Reviews Methods Primers.* **2023**, *3*.
[44] J. C. Dong, X. G. Zhang, V. Briega-Martos, X.i Jin, J.i Yang, S. Chen, Z. L. Yang, D.e-Y. Wu, J. M. Feliu, C. T. Williams, Z. Q. Tian, J. F. Li, *Nat. Energy.* **2019**, *4*, 60.
[45] G. Liu, D. Hao, K. Wang, G. Dong, X. Yu, R. Xu, M. Ji, X. Zhu, Y. Ma, L. Ma, *J. Phys. Chem. C.* **2021**, *125*, 18792.
[46] Y. Zhao, C. Xiao, E. Mejia, A. Garg, J. Song, A. Agrawal, W. Zhou, *ACS Nano.* **2023**, *17*, 8634.
[47] J. Mertens, M. E. Kleemann, R. Chikkaraddy, P. Narang, J. J. Baumberg, *Nano Lett.* **2017**, *17*, 2568.
[48] W. Nam, Y. Zhao, J. Song, S. Ali Safiabadi Tali, S. Kang, W. Zhu, H. J. Lezec, A. Agrawal, P. J. Vikesland, W. Zhou, *J. Phys. Chem. Lett.* **2020**, *11*, 9543.
[49] R. Carles, M. Bayle, P. Benzo, G. Benassayag, C. Bonafos, G. Cacciato, V. Privitera, *Phys. Rev. B.* **2015**, *92*, 174302.
[50] A. Mooradian, *Phys. Rev. Lett.* **1969**, *22*, 185.
[51] G. Boyd, Z. Yu, Y. Shen, *Phys. Rev. B.* **1986**, *33*, 7923.
[52] Y.i-Y.u Cai, J. G. Liu, L. J. Tauzin, D.a Huang, E. Sung, H. Zhang, A. Joplin, W. S. Chang, P. Nordlander, S. Link, *ACS Nano.* **2018**, *12*, 976.
[53] K. Q. Lin, J. Yi, S. Hu, J. J. Sun, J. T. Zheng, X. Wang, B. Ren, *ACS Photonics.* **2016**, *3*, 1248.
[54] C. Xiao, Y. Zhao, W. Zhou, *Nanoscale Advances.* **2021**, *3*, 556.

[55] J. Song, W. Zhou, *Nano Lett.* **2018**, *18*, 4409.
[56] M. Nie, Y. Zhao, W. Nam, J. Song, W. Zhu, H. J. Lezec, A. Agrawal, W. Zhou, *Adv. Funct. Mater.* **2022**, *32*, 2202231.
[57] F. Pargar, H. Kolev, D. A. Koleva, K. van Breugel, *J. Mater. Sci.* **2018**, *53*, 7527.
[58] E. C. Le Ru, E. Blackie, M. Meyer, P. G. Etchegoin, *J. Phys. Chem. C.* **2007**, *111*, 13794.
[59] E. Mejia, J. Song, Y. Zhao, Y. Qian, C. Xiao, H. J. Lezec, A. Agrawal, W. Zhou, *Nanoscale.* **2022**, *14*, 15373.
[60] R. Bates, J. Macaskill, *Pure Appl. Chem.* **1978**, *50*, 1701.
[61] E. J. Liang, C. Engert, W. Kiefer, *Vib. Spectrosc.* **1995**, *8*, 435.
[62] H. Setiyanto, M. Y. A. Ferizal, M. A. Zulfikar, V. Saraswaty, N. Mufti, *MSCEIS 2019: Proceedings of the 7th Mathematics, Science, and Computer Science Education International Seminar, MSCEIS 2019*, 12 October 2019, Bandung, West Java, Indonesia, **2020**, European Alliance for Innovation, p. 474.
[63] J. Croissant, J. I. Zink, *J. Am. Chem. Soc.* **2012**, *134*, 7628.
[64] G. Baffou, J. Polleux, H. Rigneault, S. Monneret, *J. Phys. Chem. C.* **2014**, *118*, 4890.
[65] S. Glaus, G. Calzaferri, *Photochem. Photobiol. Sci.* **2003**, *2*, 398.
[66] D. V. Navolotskaya, H. S. Toh, C. Batchelor-McAuley, R. G. Compton, *ChemistryOpen.* **2015**, *4*, 595.
[67] P. B. Johnson, R. W. Christy, *Phys. Rev. B.* **1972**, *6*, 4370.